ACS OMEGA

Open Access

http://pubs.acs.org/journal/acsodf

Article

Synergistic Therapy of Melanoma by Co-Delivery of Dacarbazine and Ferroptosis-Inducing Ursolic Acid Using Biomimetic Nanoparticles

Wenjun Hou,[#] Yifan Zou,[#] Jie Li, Hui Jiang, Jinyu Li, Jie Wu, Senlin Zhu, Yan Ding, Huae Xu, Feng Jia,* and Xiaolin Li*

Cite This: *ACS Omega* 2024, 9, 41532−41543

Read Online

ACCESS | Metrics & More | Article Recommendations | Supporting Information

ABSTRACT: Melanoma is one of the most aggressive types of cancer and is prone to metastasis, making current clinical treatment quite difficult. The usage of the first-line medication dacarbazine (DTIC) for melanoma is limited due to harsh side effects, limited water solubility, and a short half-life. To tackle these disadvantages, polylactic acid-hydroxyacetic acid copolymer nanoparticles (NPs) loaded with dacarbazine and ursolic acid (NPs) were fabricated, which were further encapsulated with a red blood cell membrane (RNPs). MTT, apoptosis assay, wound healing assay, colony formation assay, and immunohistochemistry were used to assess the antitumor effect of NPs and RNPs. Ferroptosis evaluation was implemented using GSH detection and the malondialdehyde assay. We found that RNPs exhibited stability and biosafety in vitro and in vivo and achieved superior anticancer ability against xenograft tumors compared with single agents and NPs, which indicated the synergistic and biomimetic efficacy. Furthermore, ferroptotic activity was observed in RNPs-treated tumor cells, and ferroptosis inhibition could partially rescue melanoma cells from RNPs-induced cell death. Collectively, this study evaluated the potential of RNPs as a novel biomimetic nanomedicine for synergistic melanoma therapy by eliciting ferroptosis in tumor cells with both anticancer activity and biosafety.

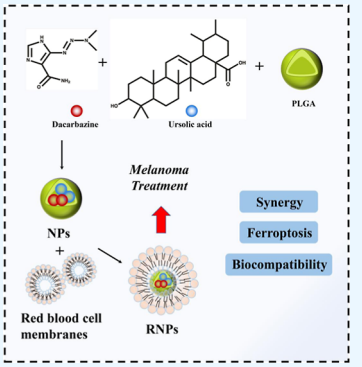

INTRODUCTION

Cancer is the main cause of mortality and a significant obstacle to extending life expectancy in every country.[1] Melanoma is a heterogeneous disease that is one of the worst kinds of metastatic cancer. The mortality and incidence of melanoma have also been rising in recent years.[2,3] Various treatment methods, including immunotherapy and molecular targeted therapy, have steadily evolved in the clinical management of melanoma, however, the tumor's immunosuppressive milieu renders the targeted medication response rate relatively poor.[4,5] Therefore, chemotherapy is still used as the best first-line cancer treatment. Nevertheless, in monotherapy with continuous chemotherapy, cancer cells can bypass the pathways affected by chemotherapeutic agents and induce drug resistance, leading to poor efficacy and recurrence, so a synergistic combination of various chemotherapeutic agents would naturally be an ideal alternative strategy.[6−8] With the development of multidrug delivery systems or multifunctional nanocarriers for synergistic multiple therapeutic modalities like photodynamic therapy, radiation therapy, and photothermal therapy, the concept of coencapsulating multiple drugs with various antitumor activities has been explored for cancer therapy.[9,10]

The application of chemotherapeutic agents for melanoma such as dacarbazine (DTIC), Temozolomide, and cisplatin depends on the clinical stage of the disease.[11] Among these chemotherapeutic drugs, DTIC is one of the most common medications for melanoma treatment,[12] which destroys cancer cells by introducing an alkyl group into their DNA. Furthermore, DTIC's utility in the treatment of melanoma is restricted by its poor water solubility; delayed, partial, and unstable absorption by the body; structural instability; and light sensitivity.[13−15] Furthermore, DTIC has a short half-life, which limits its use in conjunction with other medicines. It has nonspecific harmful effects on normal cells, with side effects such as bone marrow suppression, like other alkylating drugs.[16,17] As a result, it is urgently warranted to design an appropriate delivery method for DTIC in conjunction with other medications for targeted and efficient distribution to the tumor site and mitigating harmful side effects stemming from the drugs' physicochemical qualities. Ursolic acid (UA) (3 -hydroxy-urs-12-en-28-oic acid) is a pentacyclic triterpene acid present in many natural plants.[18] It has a wide spectrum of anticancer pharmacological actions, including tumor cell

Received: June 3, 2024
Revised: September 12, 2024
Accepted: September 17, 2024
Published: September 24, 2024

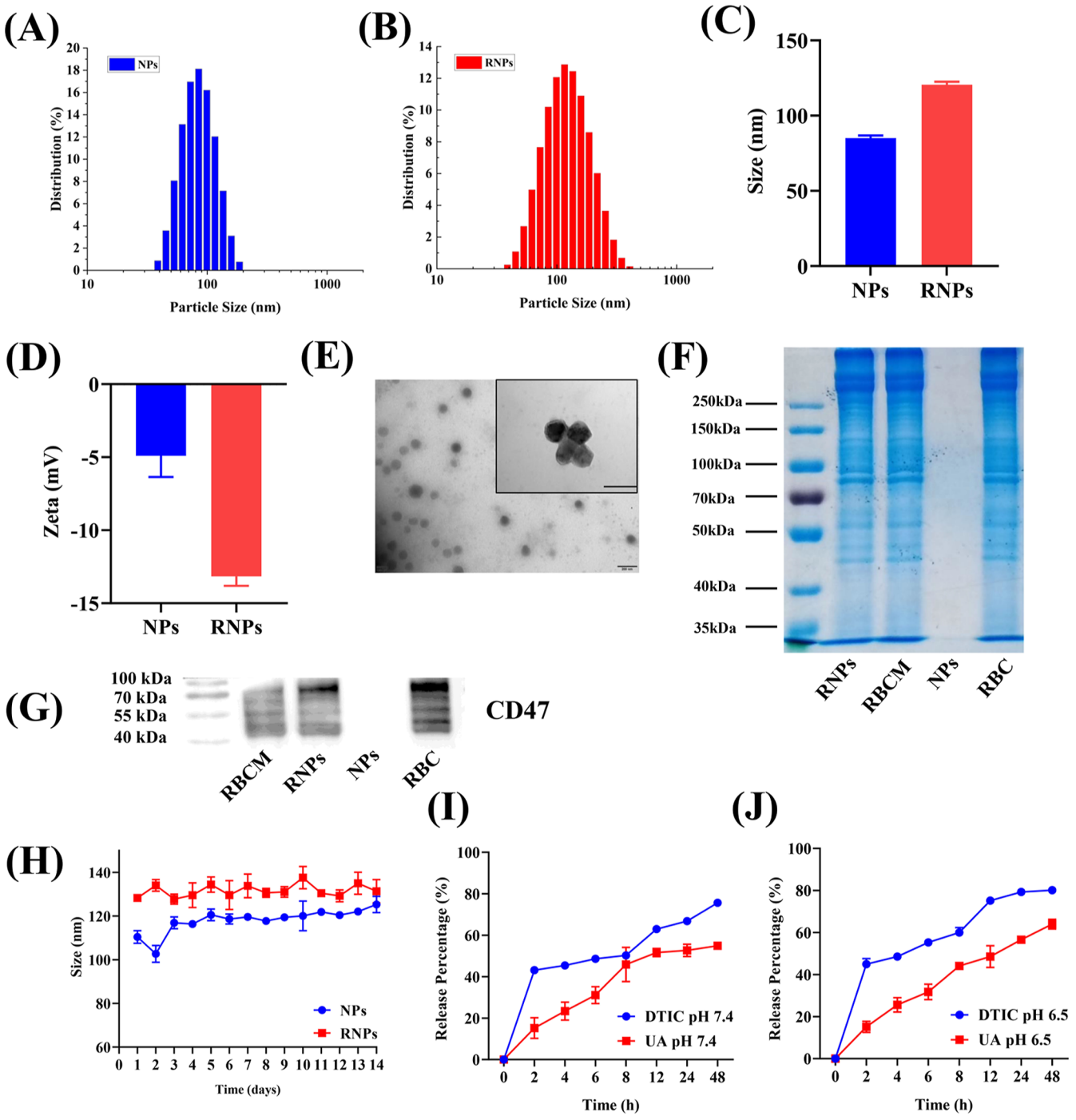

Figure 1. Characterization of fabricated nanoparticles. Size distribution images of (A) NPs and (B) RNPs. (C) Comparison between sizes of two nanoparticles. (D) Zeta potential of NPs and RNPs. (E) Images of synthesized RNPs. The scale bars represent 200 nm. (F) SDS−PAGE analysis of RNPs, RBCM, and RBC. (G)We stern blot analysis of RBCM, RNPs, NPs, and RBC for characteristic RBCM marker CD47. (H) The pattern of particle size changes of NPs and RNPs in PBS. In vitro analysis of drug release percentage under (I) pH 6.5 and (J) pH 7.4.

apoptosis induction and multidrug resistance reversal.[19,20] Previous research has indicated that UA can promote the generation of reactive oxygen species (ROS) in tumor cells,[21] but whether it can improve the therapeutic impact of DTIC is yet uncertain. In the current investigation, we studied the potential mechanism of action of UA as a synergistic medication codelivered to improve DITC cytotoxicity and overall therapeutic effect.

Polylactic acid-hydroxyacetic acid copolymer (PLGA), a biodegradable functional polymer organic compound with superior biocompatibility, nontoxicity, and capsule- and film-forming properties, is widely used in pharmaceuticals and has been officially recognized as a pharmaceutical excipient by the United States Pharmacopeia.[22−24] Various PLGA drug microspheres have been described, among which PLGA microspheres as carriers for various cancer medications is a research hotspot, thus it is critical to discover an effective drug delivery carrier based on PLGA's excellent biocompatibility and nonbiotoxicity.[25−28] In addition to concurrent extended research on drug delivery via nanomaterial carriers, academics

https://doi.org/10.1021/acsomega.4c05209
ACS Omega 2024, 9, 41532−41543

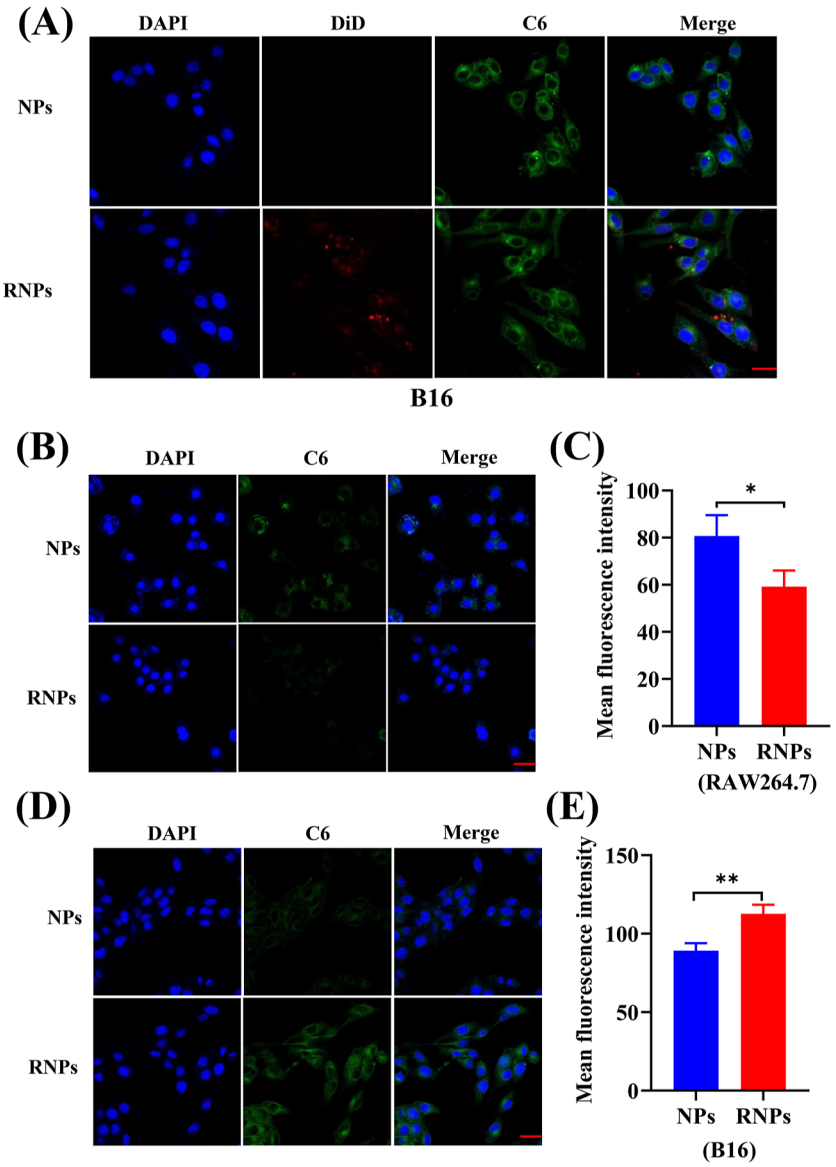

Figure 2. Confocal images demonstrating intracellular uptake peculiarity of NPs and RNPs. (A) Separate and merged images of two NPs labeled with DAPI, DiD, and C6. Scale bar = 20 μm. Images of cellular uptake patterns of NPs and RNPs in (B) RAW264.7 and (D) B16 cells. Fluorescence intensity quantified analysis of NPs and RNPs in (C) RAW264.7 and (E) B16 cells, respectively. *$p < 0.05$, **$p < 0.01$.

have presented the notion of a bionic drug delivery system based on "natural simulation", and bionic carriers are extensively employed due to their benefits in recreating the qualities of natural materials.[29,30] Cell-derived bionic carriers, in particular, have been explored due to their low immunogenicity, extended circulation duration, and strong targeting characteristics. The most typical bionic normal red blood cell membrane (RBCM)-derived nanocarriers of human cell origin may adsorb fewer plasma proteins (particularly immunoglobulins) in vivo, extend blood circulation time, efficiently penetrate dense tumor tissues, and show superb anticancer treatment effectiveness.[31−33] Therefore, after being endowed with bionic modification based on the synergistic coloading of various drug systems, the antitumor activity of PLGA nanospheres will be considerably strengthened, effectively improving the limitations of standard single-agent chemotherapy.

In the present study, considering the pharmaceutical properties of DTIC and the potential utilization of UA in melanoma treatment, we developed an erythrocyte membrane-modified PLGA dual drug delivery system, which was capable of efficiently inhibiting melanoma in vitro and in vivo by modulating the intrinsic ferroptosis-related pathways and subsequently eliciting tumor cell death, assuring biocompatibility at the same time.

RESULTS

Fabrication and Characterization of Biomimetic Nanoparticles. A biomimetic codelivery system was ingeniously designed, which includes dacarbazine and UA as therapeutic agents and PLGA and encapsulated RBCM as the drug-loading platform. A dosage ratio of 1.0:1.0 was selected for DTIC and UA based on the statistics of the drug loading content (LC) and encapsulation efficiency (Table S1). After the successful fabrication and preparation of NPs and RNPs, we first conducted an evaluation of their characterization as pharmaceuticals. The size distribution rate of NPs and RNPs was evaluated (Figure 1A,B) and the average size of

https://doi.org/10.1021/acsomega.4c05209
ACS Omega 2024, 9, 41532−41543

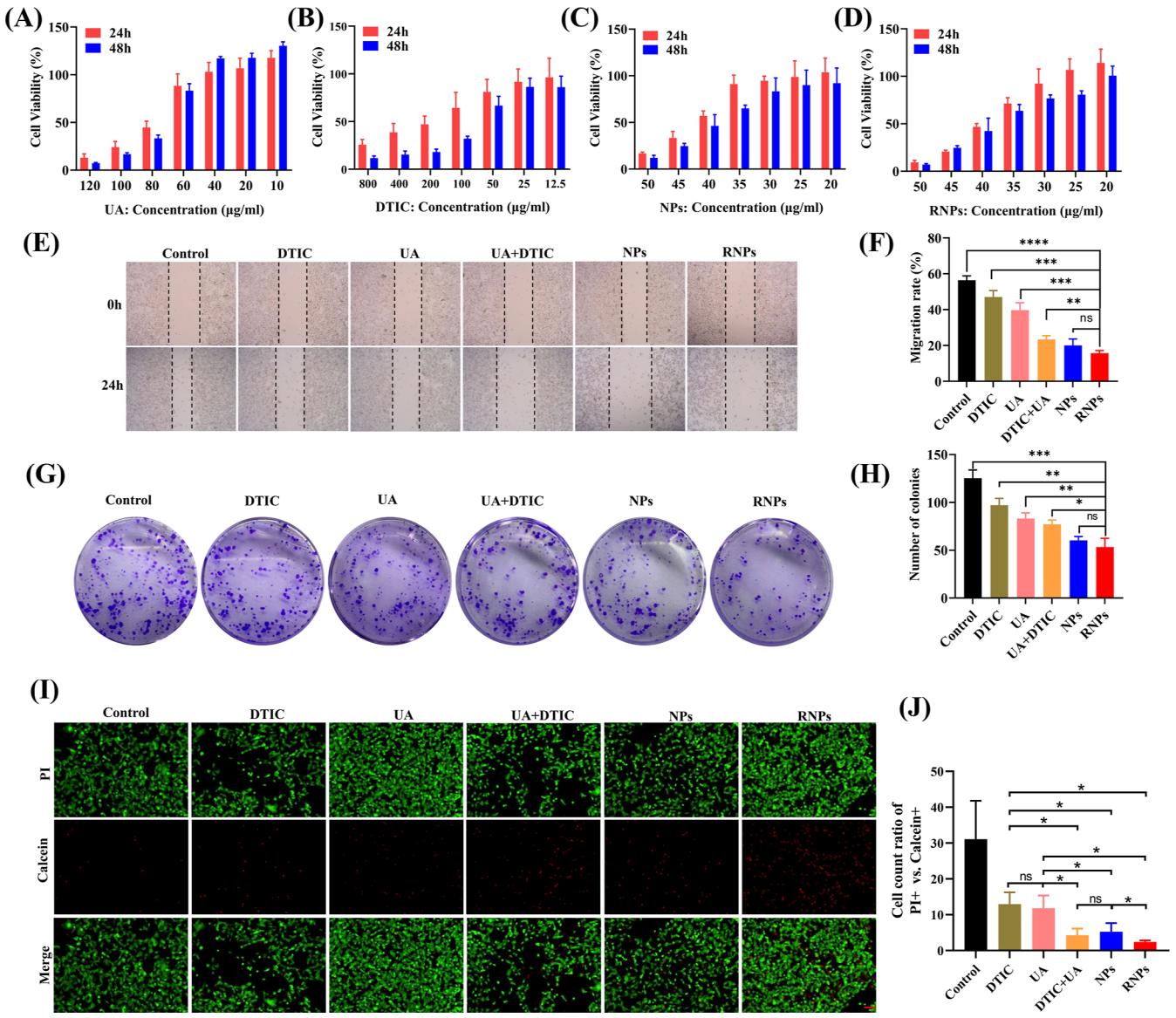

Figure 3. Anticancer effects of different kinds of drugs presented as impacts on various biological properties of B16 cells. Results of cell viability assay with the administration of four different drugs which include (A) UA, (B)DTIC, (C) NPs, and (D) RNPs. (E) Diverse effects on cell migration and (F) parallel quantified analysis of MR. (G) Clonogenicity assay images and (H) the bar chart of its counting result. (I) Outcomes of calcein/PI staining and (J) semiquantitative analysis. Scale bar = 50 μm. ns means no statistical significance, *p < 0.05, **p < 0.01, ***p < 0.001, ****p < 0.0001.

NPs was calculated as 85.1 nm, which increased to 120.6 nm after being coated within RBCM (Figure 1C). The zeta potential of NPs and RNPs was measured respectively as −4.91 and −13.16 mV (Figure 1D). Transmission electron microscopy (TEM) images indicated that RNPs presented a unilaminar layer enclosing the synthesized nanospheres (Figure 1E). The increase in RNP particle diameter and negative surface charge as well as the morphological evidence verified the successful wearing of the "invisible suit" of the RBCM.

Protein contents of RNPs, RBCM, and pure red blood cells were extracted and examined, and we found that RBCM proteins almost remained unchanged and the membrane retained on the surface of NPs (Figure 1F). We also observed that the expression of CD47, which is crucial to the immune suppressive effect that RBCM exhibits in the delivery system, was stable during the entire manufacturing process and retained its absence in NPs (Figure 1G). Furthermore, in vitro size change and drug release of the nanodrug platform were investigated. The size change patterns of NPs and RNPs were both generally similar and stable (Figure 1H), which correlated the results of in vivo pharmacokinetics in that both nanoparticles (NPs) exhibited stable release characteristics compared with single agents (Figure S1A,B). Under the pH of 6.5 and 7.4, DTIC's release percentage was shown to rise to 40% in the first two h and then both medications released in a similar manner over the next 48 h, peaking at about 80% and 60%, respectively (Figure 1I,J). These results of in vitro and in vivo experiments suggested the potential of RNPs as a biomimetic nanodrug platform.

Cellular Uptake Features of NPs and RNPs. The cell nucleus, the RBCM, and the NPs were each labeled in a distinct color with combined picture displayed in the final panel (Figure 2A). We observed the colocalization of different

https://doi.org/10.1021/acsomega.4c05209
ACS Omega 2024, 9, 41532−41543

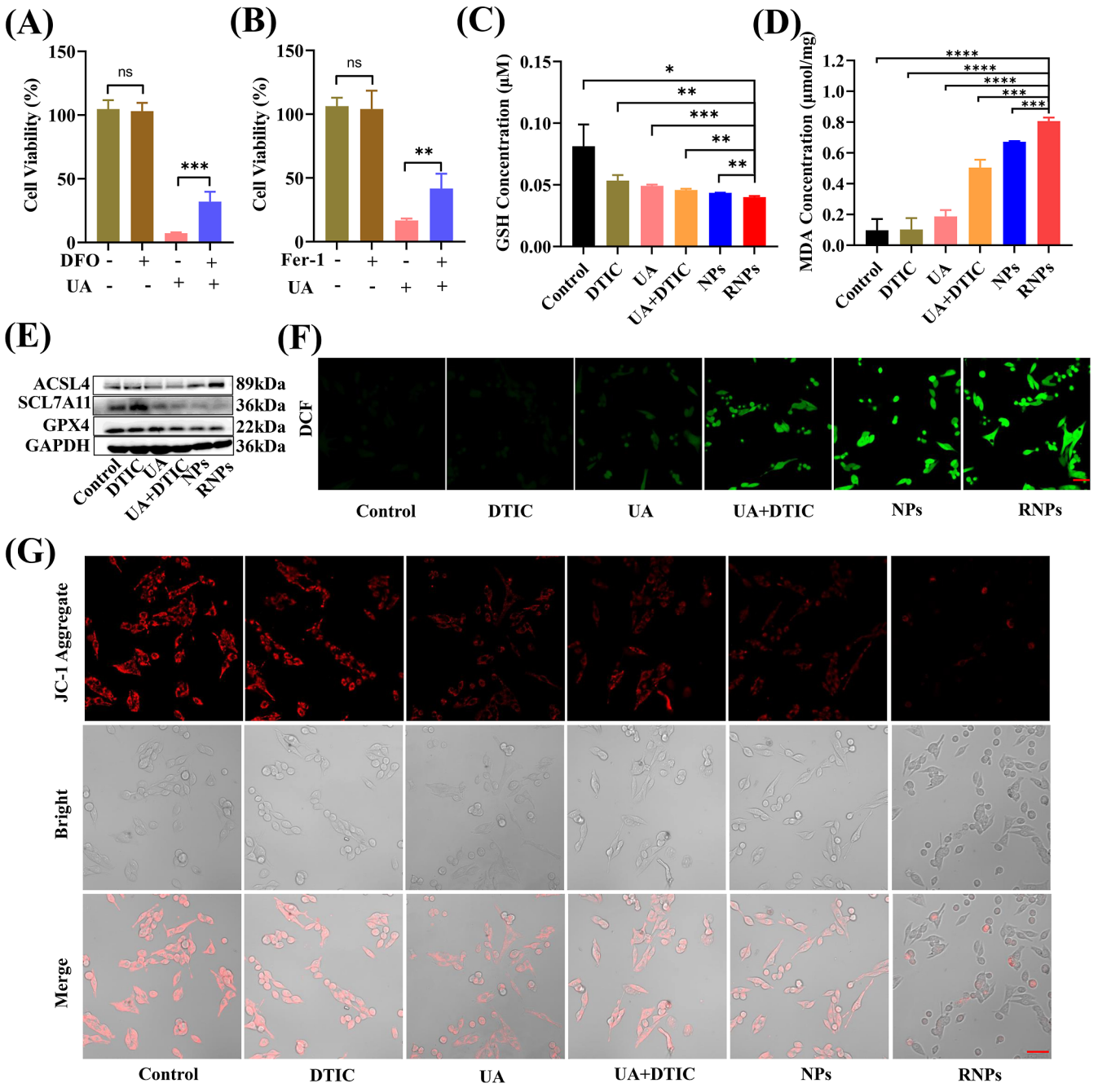

Figure 4. Evidence of occurring ferroptosis during the anticancer activity. Further cell viability assay to prove the occurrence of ferroptosis with the presence or absence of (A) DFO and (B) Fer-1. Analyses of (C) GSH and (D) MDA concentration. (E) Western blotting assay of ferroptosis marker proteins of ACSL4, SCL7A11, and GPX4. (F) Intracellular ROS levels with different ways of treatment. Scale bar = 10 μm. (G) Detection of MMP (ψ) in melanoma cells. Scale bar = 10 μm. ns means no statistical significance, $^{**}p < 0.01$, $^{***}p < 0.001$, $^{****}p < 0.0001$.

signals in both NPs and RNPs groups, suggesting the uptake of NPs by tumor cells. We also characterized the cellular uptake features of two NPs in two cell types, and we found that the phagocytotic effect of macrophages was suppressed when they encountered RNPs (Figure 2B,C) while greater fluorescent intensity was observed in tumor cells, indicating more NPs were taken in, particularly by cancer cells (Figure 2D,E). These results were further validated by flow cytometry experiments (Figure S2A,D), suggesting that the RNPs could partly evade macrophage phagocytosis and exhibited superior tumor uptake.

Influence of NPs on Cell Viability and Apoptosis. The dose range of UA and combined use of two drugs for prospective efficacy was evaluated beforehand (Figure S3A,B). We confirmed the synergistic pharmaceutical effect of two drugs under two conditions of concentration with the combination index calculated as 0.96 and 0.82, respectively (Figure S3C). B16 cells were applied with four different drugs of UA, DTIC, NPs, and RNPs and we observed that the antitumor efficacy of four agents was notable in a dose- and time-dependent manner (Figure 3A–D). We observed that NPs and RNPs could both inhibit the migration of tumor cells more effectively compared with the other groups (Figure

https://doi.org/10.1021/acsomega.4c05209
ACS Omega 2024, 9, 41532−41543

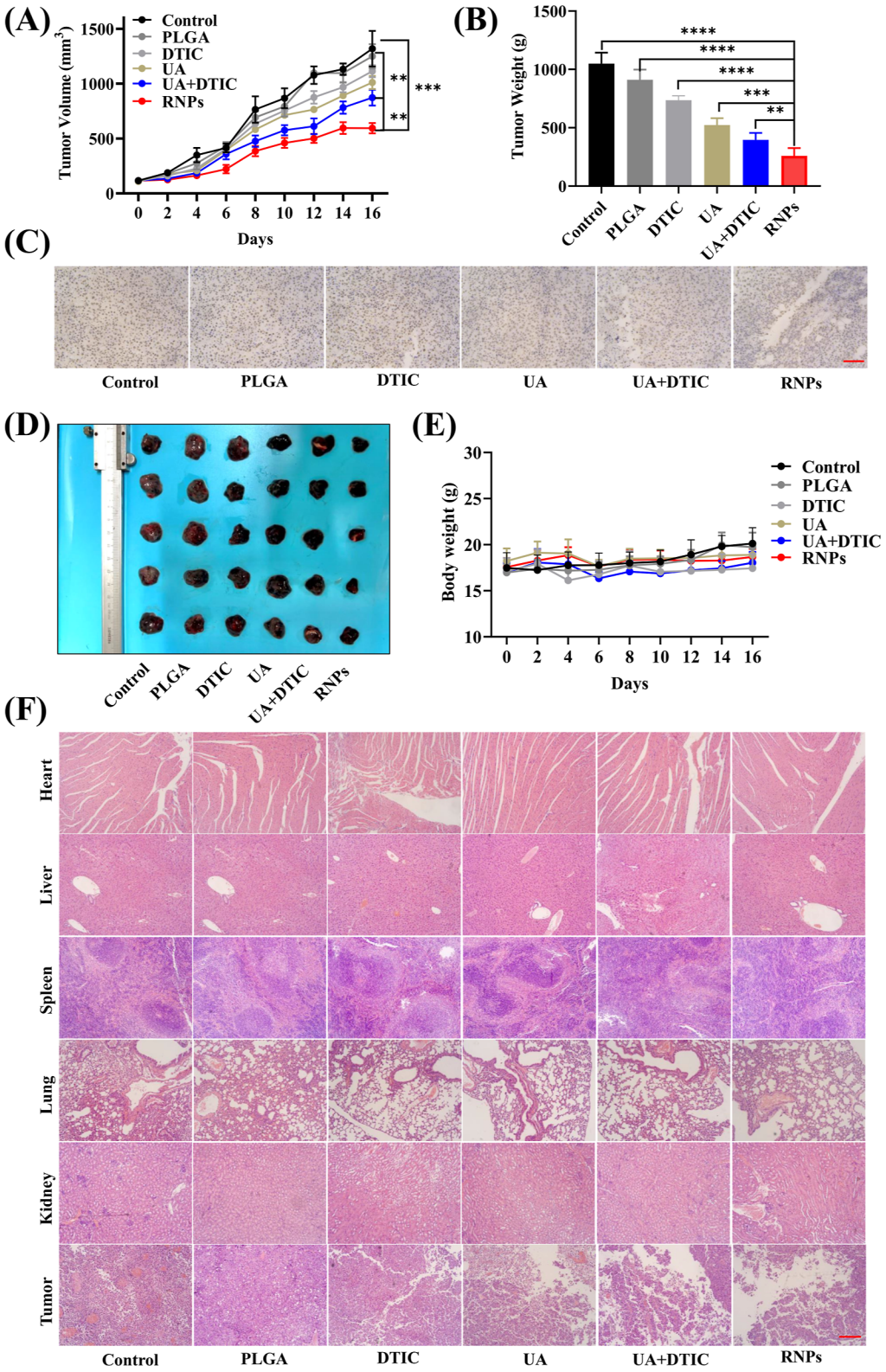

Figure 5. In vivo efficacy of NPs and RNPs against B16 melanoma and the biosafety assessment. (A) Alteration of tumor volume and (B) Tumor weight in all groups during treatment. (C) Images of fluorescent IHC incubated with K_i-67 antibody. Scale bar = 50 μm. (D) Images of tumors resected. (E) Changes in body weight of nude mice. (F) Results of hematoxylin−eosin staining of different organs in nude mice treated with NPs. Scale bar = 100 μm. $^{**}p < 0.01$, $^{***}p < 0.001$, $^{****}p < 0.0001$.

3E,F). We also confirmed the similar antitumor capacities of RNPs relative to other groups regarding proliferative inhibition (Figure 3G,H). As depicted in Figure 3I,J, NPs, RNPs, and UA + DTIC displayed substantial cellular killing effect compared with those of other groups. The results suggested that the UA and DTIC combination produced the synergistic impact.

Verification of Ferroptosis Underlying NPs and RNPs. Ferrostatin-1 (Fer-1) and deferoxamine (DFO) are two

https://doi.org/10.1021/acsomega.4c05209
ACS Omega 2024, 9, 41532−41543

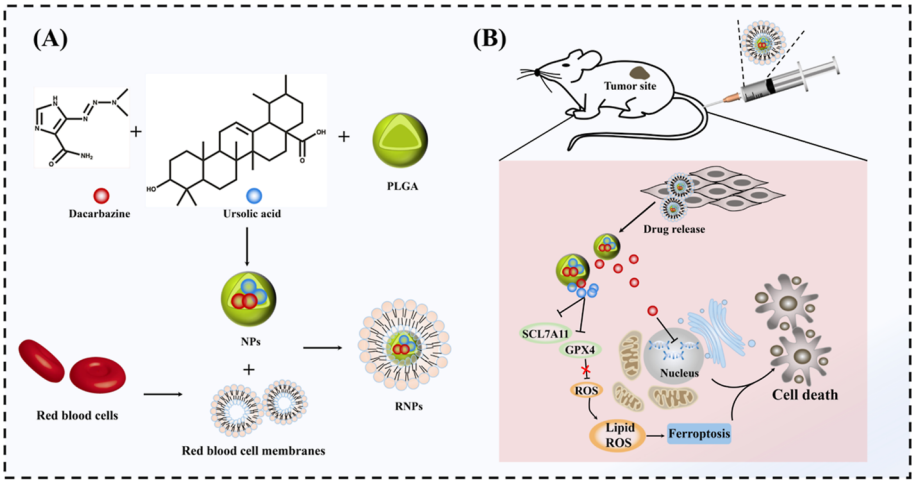

Figure 6. Schematic illustration of (A) preparation of a biomimetic codelivery system and (B) molecular mechanisms associated with the regulation of drug release from the system into the tumor site as well as the nanomedicine-induced ferroptosis of tumor cells.

effective ferroptosis inhibitors that may prevent peroxidation processes initiated by iron in ferroptosis.[34] Both ferroptosis inhibitors did not elicit cell death but partially rescued the antitumor effect of UA, indicating that ferroptosis plays a fundamental role in the mechanism of UA cytotoxicity (Figure 4A,B).

According to the existing research, the complicated process of ferroptosis would entail lipid peroxidation into MDA and the prevention of this procedure is partially dependent on GSH production.[35] In the present study, the application of RNPs could significantly induce lower GSH levels and higher MDA levels compared with those of other groups (Figure 4C,D). Three biomarker proteins (ACSL4, SLC7A11, and GPX4) for ferroptosis were examined, and we observed that the positive regulator ACSL4 was significantly elevated while two negative marker proteins (SLC7A11 and GPX4) were both remarkedly downregulated with the confirmation of quantitative analysis (Figures 4E and S4A−C). It should be noted that ferroptosis cell death is attributed to oxidative damage, which is directly triggered by certain types of ROS.[36] Measurement of ROS was performed with the fluorescence of dichlorofluorescein (DCF) and we found that cells coincubated with NPs and RNPs generated a substantially higher amount of ROS (Figure 4F). Furthermore, ferroptosis is also frequently associated with the degradation of mitochondrial structure and function and the mitochondrial membrane potential (MMP) was measured by JC-1 staining.[37] We observed that there was a low intensity of red fluorescence in the RNPs group, indicating that the drug might induce the onset of ferroptosis by causing enormous damage to mitochondria (Figure 4G). Considering the biomarkers tested above in the treated B16 cells, we speculated that ferroptosis was primarily responsible for the anticancer effect observed in the action process of NPs and RNPs.

In Vivo Therapeutic and Biocompatibility Evaluation. B16 cell tumor-bearing nude mice were randomly separated into six groups for in vivo antitumor effect assessment. We found that the RNPs elicited the best tumor growth inhibition and resulted in the lowest average tumor weight compared with other therapeutic agents and control group (Figure 5A,B). A higher percentage of K_i-67 positive cells from immunohistochemical (IHC) staining indicates more rapid tumor growth and a worse prognosis, and we observed that the expression of K_i-67 was obviously decreased after effective drug therapy with all the treatment groups, especially in the RNPs group (Figure 5C). The therapeutic effectiveness of RNPs was further confirmed by pictures of tumor mass, which showed a substantially decreased tumor volume compared to other groups (Figure 5D). The above findings suggested that RNPs had a superior antitumor impact and could efficiently suppressed tumor development and progression in vivo.

The measurement of body weight of mice and H&E staining of major organs were utilized to examine systemic safety and biocompatibility of different therapeutical drugs. We found that all groups of mice generally maintained their body weight, indicating that there was no obvious systemic toxicity during the treatment (Figure 5E). The tissue H&E staining photos revealed that the administration of all therapeutic medicines as well as PLGA would cause no significant damage to key organs, including the heart, liver, spleen, lung, and kidney (Figure 5F).

In summary, as illustrated in Figure 6A, an antimelanoma biomimetic drug delivery system was designed and prepared. The RNPs exhibited significant antitumor activity against cell viability, migration capacity, and clonogenic ability in vitro, as well as growth speed in tumor-bearing xenograft mice. We also observed that the synergistic anticancer effect derived from UA could be attributed to its ability to elicit ferroptosis in tumor cells, which proposed a novel mechanism underlying UA's pharmaceutical potency (Figure 6B). These results together suggested that the nanomedicine of RNPs obtained better anticancer performance with the fewest unwanted side effects and proved a promising antimelanoma candidate ensuring both efficacy and biosafety.

DISCUSSION

Melanoma is a common malignancy whose incidence rates are rising, particularly in white populations, posing a great threat to global health.[38] Despite the advances in immunotherapy and surgical management, DTIC remains a major chemotherapeutic drug for advanced and metastatic melanoma, commonly utilized alone or combined with immune checkpoint blockade or target therapy.[39−41] However, considering its toxicity to normal organs, poor solubility, photosensitivity, and instability in vivo, better drug delivery strategy and adjuvant drugs are urgently needed to improve the biocompatibility and efficacy of DTIC. In the present study, we discovered that the combination of DTIC and UA with RBCM and PLGA delivery

https://doi.org/10.1021/acsomega.4c05209
ACS Omega 2024, 9, 41532−41543

system exerted a synergistic antitumor effect against melanoma B16 cells with enhanced delivery efficiency and attenuated macrophagic elimination.

Ferroptosis is a novel cell death driven by iron-dependent phospholipid peroxidation and, therefore, ferroptosis-related metabolic pathways could be targeted and manipulated to potentiate cancer treatment clinically.[34,42] Previous studies have reported that the application of UA could function as an auxiliary therapeutic drug for sorafenib and induce ferroptotic death in various cancer types, including liver, lung, breast, colon, gastric, and prostate cancer.[21] However, the role of UA in treating melanoma and whether it could also function by eliciting ferroptosis remains unclear. In our study, three proteins (ACSL4, SLC7A11, and GPX4) were selected and detected as biomarkers during ferroptosis. ACSL4 functions as a positive regulator in structuring cellular phospholipids during lipid metabolism dysregulation and GPX4 in the membrane can directly convert lipid hydroperoxide to equivalent lipid alcohol, whose inactivation would accelerate the process of lipid peroxidation and finally result in ferroptosis.[36] Also, SLC7A11 functions as a reverse regulator of ferroptosis by participating in the formation of the cystine/glutamate antiporter (System X_C^-), which can regulate ferroptosis by navigating cystine entering cells and dysfunction of the pathway directly leads to the blockade of GSH synthesis.[43] Other ferroptotic biomarkers including MDA, GSH, and MMP were examined as well, and we confirmed the onset of ferroptosis after UA treatment.

Furthermore, we developed the combined therapeutic NP of RNPs in a biomimetic drug delivery platform composed of PLGA and RBCM, which was proved to improve drug delivery efficiency and augment biocompatibility compared to single agents. As expected, RNPs predominately exhibited superior potency compared to NPs, which could be explained by the membrane proteins of the RBCM mediating the protective effect of evading immune-induced clearance by macrophages. Among these proteins, it is previously documented that CD47, which possesses a "do not eat me" signal and therefore immune-evading property, plays a significant role in suppressing phagocytosis.[44] Therefore, RAW 264.7 cells demonstrated significantly less intracellular uptake of RNPs than NPs and it was further confirmed that RNPs exhibited more cellular uptake by cancer cells than NPs, both indicating the intrinsic biocompatibility of RNPs. The encapsulation of RBCMs on the surface of the NPs might help them escape the clearance of phagocytosis and subsequently prolong the blood half-life, resulting in more effective therapeutic ingredients arriving at tumor sites and exerting tumor-inhibiting activity.

Nevertheless, several limitations still exist in this study. First, all experiments in the present study were implemented in vitro or in nude mice, which could not fully reflect the antitumor or biotoxicity effect of RNPs and NPs inside human bodies, and further experiments in other animal models are warranted. Furthermore, the pharmaceutical mechanism of UA should be revisited, because its anticancer effect could only be partially attributed to ferroptosis according to the results. Ferroptosis combined with other forms of cell death, including apoptosis and autophagy, might contribute to the antitumor effect together. We suggested that the cell death mechanism should be explored in an intact manner. Finally, it is also worth noting that the tumor immune microenvironment plays a major part in cancer progression and therapeutic resistance.[45,46] Considering that immune and myeloid cells in the tumor ecosystem are subject to the ferroptotic modulation[47,48] and may influence the curative effect of RNPs, experiments in immunocompetent mice and other immuno-oncology animal models are further warranted.

CONCLUSIONS

Collectively, we created a drug delivery platform comprising PLGA, UA, and DTIC for the treatment of melanoma, intending to achieve high targeting efficiency while minimizing toxicity. During the in vitro experiment, we assessed the NP's characteristics as well as its therapeutic effectiveness against B16 cells and discovered that ferroptosis played an important part in the therapeutic process. In vivo testing confirmed the antitumor effect and biocompatibility of RNPs as potential chemotherapy drug. We can conclude that with further structural optimization and trials, the NP agent can be qualified as a promising chemotherapeutic drug against melanoma.

METHODS

Materials. Dacarbazine (≥99.0%), UA (≥99.0%), and Coumarin-6 (C6) (≥98.0%) were purchased from Macline Biochemical Technology Co. (Shanghai, China). 1,1′-Dioctadecyl-3,3,3′,3′-tetramethylindodicarbocyanine, 4-Chlorobenzenesulfonate (DiD), detergent-compatible Bradford protein assay kit, Coomassie Blue staining solution, and 3-(4,5-dimethyl-2-thiazolyl)-2,5-diphenyl-2-*H*-tetrazolium bromide (MTT) and Calcein-AM/PI Double Stain Kit Calcein-AM/ were purchased from Beyotime Biotechnology Co. (Nantong, China). Crystalline violet staining solution and 4% paraformaldehyde were purchased from Fcmcs Biologicals (Nanjing, Jiangsu, China); ROS Assay Kit and MMP assay kit were purchased from Eisen (Shanghai, China).

Cell Lines and Animals. B16 cells were purchased from Shanghai Fuheng Biotechnology Co., Ltd. Mouse macrophage RAW264.7 cells were obtained from the Institute of Biochemistry and Cell Biology, Shanghai Institute of Biological Sciences, Chinese Academy of Sciences (Shanghai, China). Cells were incubated in a constant temperature incubation oscillator (Shanghai Zhicheng Analytical Instrument Manufacturing Co., Ltd., China) if not mentioned otherwise. Female nude mice 4−6 weeks old were obtained from the Animal Core Facility of Nanjing Medical University. All animal experimental procedures were approved by the Nanjing Medical University Ethics Committee for Animal Laboratory Research and followed the guidelines of ethical regulations for institutional animal care and use at Nanjing Medical University (approval number: 2104050).

Preparation of NPs. The nanomedicine was manufactured by a previously reported method.[49] In brief, a certain amount of PLGA (30 mg), DTIC (6 mg), and UA (6 mg) was dissolved in 1 mL of dichloromethane as the organic phase, and PVA solution was prepared as the aqueous phase. The former was emulsified with a PVA solution. With constant stirring for 4 h at room temperature, the organic solvent in the obtained suspension was evaporated and subsequently centrifuged to harvest the precipitate of target NPs. The C6-labeled PLGA NPs (C6-NPs) were prepared with a similar method except for the replacement of two drugs with 0.1 wt % C6.

Isolation and Purification of RBCMs. Several healthy mice were selected for the collection of fresh whole blood. The

https://doi.org/10.1021/acsomega.4c05209
ACS Omega 2024, 9, 41532−41543

extracted sample was centrifuged at 300*g* for 5 min (4 °C). The sedimentation was washed with 1 × phosphate buffered saline (PBS, pH 7.4) two times followed by the lysis of deposit red blood cells with 0.25 × PBS for 30 min on ice. The cell solution was centrifuged at 7000*g*, 15 min (4 °C). Then the harvested precipitate was resuspended in 0.25 × PBS. The obtained solution was stored in deionized water at −80 °C.

Preparation of RNPs. The fabrication of RBCM-cloaked NPs was completed according to a protocol of the sonication method. The RBCM solution was added to NPs in liquid condition, and the mixture was ultrasonicated in ice water for 20 min to coat the surface of NPs and obtain RBCM-cloaked NPs (RNPs).

Characterization of NPs. The size and zeta potential of two types of fabricated particles were measured by dynamic light scattering (DLS), respectively, and the morphological features were then observed by TEM (JEOL JEM-1010328 electron-microscope, Japan). To further verify the RBCM coated on NPs, three agents were extracted, respectively, for the detection of their contents. The concentration of each sample was calculated using a BCA protein quantification kit and adjusted. Then, the samples were characterized by 10% sodium dodecyl sulfate (SDS)−polyacrylamide gel, which was stained with Coomassie brilliant blue following electrophoresis, and imaged to visualize protein bands.

Detection of Drug Loading and Encapsulation Efficiency. High-performance liquid chromatography (HPLC; Shimadzu, Japan) was employed to quantify the drug loading and encapsulation of DTIC and UA. The same quantity of methanol was added into the NP solution, vortex for demulsification, and then the mixture was centrifuged with a high-speed refrigerated centrifuge (Thermo Fisher Scientific, USA). After demulsification, DTIC and UA encapsulated in the core were analyzed, respectively. The drug LC and entrapment efficiency (EE) were calculated by the following equation as follows

$$\text{LC } \% = (\text{mass of drug in NPs})/(\text{total mass of RNPs}) \times 100\% \quad (1)$$

$$\text{EE } \% = (\text{mass of drug in NPs})/(\text{total mass of drug in feed}) \times 100\% \quad (2)$$

In Vitro Stability and Drug Release Analysis. NPs and RNPs were dissolved in PBS (pH 6.5) respectively and incubated at 37 °C. Samples were taken daily for 2 weeks, and the sizes of both particles were measured by DLS. RNPs were encapsulated in dialysis bags and immersed in PBS (pH 6.5) while shaking at 150 rpm for 48 h at 37 °C. The amount of released DTIC and UA was measured by HPLC.

Co-Localization Analysis and Cellular Uptake Assay. B16 cells (2×10^5 cells/dish) were seeded in confocal dishes and incubated at 37 °C for 24 h, after which culture media containing DiD-labeled RNPs was added, followed by incubation for 4 h at 37 °C. After removing the culture media, the plate was washed with PBS and the cells left were fixed with 4% paraformaldehyde. After staining with 4′,6-diamidino-2-phenylindole (DAPI), the cells were observed using a confocal laser scanning microscope (CLSM; ZEISS LSM710, German). RAW264.7 and B16 cells were cultured in confocal dishes. The cells were then applied with C6-NPs and C6-RNPs and incubated for 24 h. Then, DAPI was applied, and the location of nuclei. All samples were observed by a confocal microscope and detected by flow cytometry.

MTT Assay. B16 cells were inoculated into 96-well plates (5×10^3 cells/well). After 24 h, each well was treated with UA, DTIC, NPs and RNPs and incubated for 24 and 48 h. Then, cells were incubated with MTT working solution and added to a dimethyl sulfoxide solution. The absorbance at 492 nm was determined with a microplate reader and cell viability rates was calculated. The assay was repeated under several conditions where cells were administrated with UA with or without the presence of Fer-1 and DFO.

Apoptosis Assay. A cytotoxicity assay kit was employed to further explore the cytocidal effects of drugs. B16 cells were inoculated in 12-well plates and were treated as mentioned above. The supernatant was removed, and the culture plate was washed with 1 × PBS. Subsequently, each well was applied with 500 μL Calcein AM/PI working solution and incubated for 30 min. The 12-well plates were observed under a fluorescence microscope (Leica DM2500).

Cell Wound Healing Assay. B16 cells were inoculated into 6-well plates overnight, and the bottom of 6-well plates was subsequently scratched with a 200 μL pipet tip. Next, cells were incubated with complete medium, UA, DTIC, UA + DTIC, NPs, and RNPs separately for 24 and 48 h. Cell images were subsequently captured under an inverted biological microscope (Nanjing Jiangnan Yongxin Optical Co., Ltd., China) and the migration rate (MR) was calculated.

Colony Formation Assay. B16 cells were seeded in a six-well plate at a density of 800 cells/well. When the cells are adherent, they were subjected to the application of complete medium, UA, DTIC, UA + DTIC, NPs, and RNPs separately, and the incubation lasted for 24 h. After the procedure, the drug-containing supernatant was discarded, replaced with fresh medium, and incubated for 2 weeks. After 14 days, viable cells growing into colonies were gently washed with prechilled PBS and fixed with 4% paraformaldehyde. Next, samples were dyed with 0.5% crystal violet for 15 min. Colony numbers were calculated according to the photograph of each well and prepared for further statistical analysis.

GSH Detection and Malondialdehyde Assay. Reduced glutathione (GSH) and a GSSG Assay Kit (Beyotime) were employed for the detection of GSH levels. All solutions were prepared according to the guidance. The cells previously treated with complete medium, UA, DTIC, UA + DTIC, NPs, and RNPs were added with a protein removal reagent M solution. Then we used liquid nitrogen and a 37 °C water bath to freeze and thaw the sample twice. The solution was then centrifuged, and the supernatant was mixed with 150 μL of total glutathione detection working solution. The mixture was incubated before 50 μL of 0.5 mg/mL NADPH solution was added for the determination of A412 with a microplate reader (Tannon, China). The content of GSH was then reckoned according to the standard curve and absorbance value. Lipid Peroxidation MDA Assay Kit (Beyotime) was employed for the detection of MDA levels according to the manufacturer's instructions.

Detection of Intracellular ROS. A ROS assay kit (Boxbio, Beijing) containing DCF was purchased to detect intracellular ROS and evaluate the effect of different drugs. All the procedures were completed according to the manufacturer's instructions.

Measurement of the MMP by JC-1. A MMP assay kit (Biobox, Beijing) was utilized. B16 cells previously treated with

https://doi.org/10.1021/acsomega.4c05209
ACS Omega 2024, 9, 41532−41543

complete medium, UA, DTIC, UA + DTIC, NPs, and RNPs were immersed in 1 mL of cell culture medium and 1 mL of JC-1 stain working solution. The final supernatant was discarded, and cells were washed with diluted JC-1 Dyeing Buffer (1×) 3 times before they were observed with a fluorescence microscope.

Western Blot. B16 cells treated with complete medium, UA, DTIC, UA + DTIC, NPs, and RNPs for 48 h were collected and cracked with RIPA + PMSF (100:1/v/v). 30 μg of the extracted whole protein was separated by SDS−PAGE and subsequently transferred onto the polyvinylidene fluoride (PVDF) membrane. After being blocked by 5% TBST of nonfat milk, the PVDF membrane was then incubated with the chosen primary antibody of ferroptosis marker protein at 4 °C. The corresponding secondary antibody was combined afterward and then the membrane was treated with a chemiluminescent horseradish peroxidase reagent. Finally, the strips were imaged by a ChemiDoc imaging system (Tannon, China).

In Vivo Evaluation of Antitumor Effect and Safety. Melanoma B16 cells (mouse origin) in a logarithmic growth period were selected, and tumor cells (1×10^7) in 100 μL of medium were injected under the skin on both sides of the back of female nude mice. When the bulges on the back of mice were observed and grown to 90 mm^3, they were randomly divided into 6 groups of 5 mice per group. The drugs were administrated on a daily basis. Meanwhile, body weight and tumor volumes were measured and recorded. The experimental end point was defined as either death or massive tumor size (greater than 1000 mm^3) and when that came, the lived mice were euthanized properly. The tissue of the tumor, heart, liver, spleen, lung, and kidney was collected and stored in 4% paraformaldehyde overnight, which was stained with hematoxylin and eosin (HE) then.

In Vivo Pharmacokinetics. BALB/c mice were randomly divided into three groups: (1) DTIC solution group (5 mg/kg), (2) UA group (5 mg/kg), (3) NPs group (5 mg/kg DTIC and UA), and (4) RNPs group (5 mg/kg DTIC and UA) (3 mice per group). Drugs were injected into the mice via the tail vein (0.2 mL/min). At predetermined time points of 1, 4, 8, and 24 h post injection, blood samples were collected into heparinized polyethylene tubes from the periorbital vein and centrifuged immediately at 6000 rpm for 10 min to obtain plasma. The concentrations of DTIC and UA in the plasma were assayed by HPLC.

IHC Analysis. The tissue slices were first treated with a Tris−EDTA buffer solution. After that, samples were incubated with the main antibody and Ki67. Visualization and observation ensued, which were carried out under an optical microscope. At last, the level of Ki67-positive cells was determined.

Statistical Analysis. The results were processed and displayed as means ± standard deviation. GraphPad Prism 8.0c software was employed for statistical analysis and ImageJ software for semiquantitative analysis of fluorescence images and gel bands. Student's *t*-test (two tailed) was applied in the data analysis, with a *p*-value less than 0.05 considered statistically significant. $^*p < 0.05$, $^{**}p < 0.01$, $^{***}p < 0.001$, $^{****}p < 0.0001$.

■ ASSOCIATED CONTENT

Supporting Information

The Supporting Information is available free of charge at https://pubs.acs.org/doi/10.1021/acsomega.4c05209.

The details of drug LC and encapsulation efficiency; in vivo pharmacokinetics; in vitro flow cytometry analyses; synergistic effects of two agents; and further Western blot gel band analyses (PDF)

■ AUTHOR INFORMATION

Corresponding Authors

Feng Jia − *Department of Neurosurgery, Yancheng No. 1 People's Hospital, The Affiliated Yancheng First Hospital of Nanjing University Medical School, Yancheng 224008, China*; Email: jfsjwk@163.com

Xiaolin Li − *Department of Geriatric Gastroenterology, The First Affiliated Hospital of Nanjing Medical University, Nanjing 210029, China*; orcid.org/0000-0002-7510-9735; Email: lxl@njmu.edu.cn

Authors

Wenjun Hou − *Department of Dermatology, Nanjing Drum Tower Hospital, Nanjing 210008, China*

Yifan Zou − *Department of Pharmaceutics, School of Pharmacy, Nanjing Medical University, Nanjing 211166, China; Department of General Surgery, The First Affiliated Hospital of Nanjing Medical University, Nanjing 210029, China*; orcid.org/0000-0002-5876-9766

Jie Li − *Department of Geriatric Gastroenterology, The First Affiliated Hospital of Nanjing Medical University, Nanjing 210029, China*

Hui Jiang − *Department of Pharmaceutics, School of Pharmacy, Nanjing Medical University, Nanjing 211166, China*

Jinyu Li − *Department of Pharmaceutics, School of Pharmacy, Nanjing Medical University, Nanjing 211166, China*

Jie Wu − *Department of Pharmaceutics, School of Pharmacy, Nanjing Medical University, Nanjing 211166, China*

Senlin Zhu − *Department of Pharmaceutics, School of Pharmacy, Nanjing Medical University, Nanjing 211166, China*

Yan Ding − *Department of Geriatric Gastroenterology, The First Affiliated Hospital of Nanjing Medical University, Nanjing 210029, China*

Huae Xu − *Department of Pharmaceutics, School of Pharmacy, Nanjing Medical University, Nanjing 211166, China*; orcid.org/0000-0001-9124-303X

Complete contact information is available at: https://pubs.acs.org/10.1021/acsomega.4c05209

Author Contributions

#W.H. and Y.Z. contributed equally to this paper. W.H and Y.Z: investigation, data curation, and writing—original draft. J.L, J.L, J.W, S.Z, H.J, and Y.D: validation and writing—review and editing. X.L, F.J, and H.X: conceptualization, supervision, and funding acquisition.

Funding

This work is supported by the National Natural Science Foundation of China (82073308, 81871942, 81773211, and 82373105), the High-level startup fund of Nanjing Medical University (KY109RC2019010), and 333 Project of Jiangsu Province (BRA2020210).

Notes

The authors declare no competing financial interest.

■ ACKNOWLEDGMENTS

We would like to thank the core facility from the Department of Pharmacy of Nanjing Medical University for their help in the implementation of all experiments.

■ REFERENCES

(1) Bray, F.; Laversanne, M.; Weiderpass, E.; Soerjomataram, I. The ever-increasing importance of cancer as a leading cause of premature death worldwide. *Cancer* **2021**, *127* (16), 3029−3030.
(2) Long, G. V.; Swetter, S. M.; Menzies, A. M.; Gershenwald, J. E.; Scolyer, R. A. Cutaneous melanoma. *Lancet* **2023**, *402* (10400), 485−502.
(3) Brunsgaard, E. K.; Wu, Y. P.; Grossman, D. Melanoma in skin of color: Part I. Epidemiology and clinical presentation. *J. Am. Acad. Dermatol.* **2023**, *89* (3), 445−456.
(4) Long, G. V.; Menzies, A. M.; Scolyer, R. A. Neoadjuvant Checkpoint Immunotherapy and Melanoma: The Time Is Now. *J. Clin. Oncol.* **2023**, *41* (17), 3236−3248.
(5) Luke, J. J.; Flaherty, K. T.; Ribas, A.; Long, G. V. Targeted agents and immunotherapies: optimizing outcomes in melanoma. *Nat. Rev. Clin. Oncol.* **2017**, *14* (8), 463−482.
(6) Chudy, M.; Tokarska, K.; Jastrzębska, E.; Bułka, M.; Drozdek, S.; Lamch, Ł.; Wilk, K. A.; Brzózka, Z. Lab-on-a-chip systems for photodynamic therapy investigations. *Biosens. Bioelectron.* **2018**, *101*, 37−51.
(7) Lamch, Ł.; Pucek, A.; Kulbacka, J.; Chudy, M.; Jastrzębska, E.; Tokarska, K.; Bułka, M.; Brzózka, Z.; Wilk, K. A. Recent progress in the engineering of multifunctional colloidal nanoparticles for enhanced photodynamic therapy and bioimaging. *Adv. Colloid Interface Sci.* **2018**, *261*, 62−81.
(8) Yang, H.; Chen, Y.; Chen, Z.; Geng, Y.; Xie, X.; Shen, X.; Li, T.; Li, S.; Wu, C.; Liu, Y. Chemo-photodynamic combined gene therapy and dual-modal cancer imaging achieved by pH-responsive alginate/chitosan multilayer-modified magnetic mesoporous silica nanocomposites. *Biomater. Sci.* **2017**, *5* (5), 1001−1013.
(9) Lamch, Ł.; Kulbacka, J.; Pietkiewicz, J.; Rossowska, J.; Dubińska-Magiera, M.; Choromańska, A.; Wilk, K. A. Preparation and characterization of new zinc(II) phthalocyanine - Containing poly(l-lactide)-b-poly(ethylene glycol) copolymer micelles for photodynamic therapy. *J. Photochem. Photobiol., B* **2016**, *160*, 185.
(10) Pucelik, B.; Arnaut, L. G.; Stochel, G.; Dąbrowski, J. M. Design of Pluronic-Based Formulation for Enhanced Redaporfin-Photodynamic Therapy against Pigmented Melanoma. *ACS Appl. Mater. Interfaces* **2016**, *8* (34), 22039.
(11) Sun, H.; Chen, Y.; Chen, Y.; Liu, D.; Yan, Z.; Bin, M.; Zhao, G.; Pan, Z.; Li, Q. Primary malignant melanoma of the cervix: 14 cases and literature overview. *Melanoma Res.* **2018**, *28* (6), 578−585.
(12) Hafeez, A.; Kazmi, I. Dacarbazine nanoparticle topical delivery system for the treatment of melanoma. *Sci. Rep.* **2017**, *7* (1), 16517.
(13) Piotrowska, A.; Wierzbicka, J.; Rybarczyk, A.; Tuckey, R. C.; Slominski, A. T.; Żmijewski, M. Vitamin D and its low calcemic analogs modulate the anticancer properties of cisplatin and dacarbazine in the human melanoma A375 cell line. *Int. J. Oncol.* **2019**, *54* (4), 1481−1495.
(14) Demetri, G. D.; Schöffski, P.; Grignani, G.; Blay, J. Y.; Maki, R. G.; Van Tine, B. A.; Alcindor, T.; Jones, R. L.; D'Adamo, D. R.; Guo, M.; Chawla, S. Activity of Eribulin in Patients With Advanced Liposarcoma Demonstrated in a Subgroup Analysis From a Randomized Phase III Study of Eribulin Versus Dacarbazine. *J. Clin. Oncol.* **2017**, *35* (30), 3433−3439.
(15) Ohtsubo, T.; Tsuji, T.; Umeyama, T.; Sudou, M.; Komesu, K.; Matsumoto, M.; Yoshida, Y.; Banno, R.; Tomogane, K.; Fujita, A.; Kohno, T.; Mikami, T. [Consideration of Preventing Local Venous Pain by Dacarbazine]. *Yakugaku Zasshi* **2017**, *137* (3), 363−369.
(16) Kaplan, M. G. Ipilimumab plus dacarbazine in melanoma. *N. Engl. J. Med.* **2011**, *365* (13), 1256.
(17) Nathan, P.; Hassel, J. C.; Rutkowski, P.; Baurain, J. F.; Butler, M. O.; Schlaak, M.; Sullivan, R. J.; Ochsenreither, S.; Dummer, R.; Kirkwood, J. M.; Joshua, A. M.; Sacco, J. J.; Shoushtari, A. N.; Orloff, M.; Piulats, J. M.; Milhem, M.; Salama, A. K. S.; Curti, B.; Demidov, L.; Gastaud, L.; Mauch, C.; Yushak, M.; Carvajal, R. D.; Hamid, O.; Abdullah, S. E.; Holland, C.; Goodall, H.; Piperno-Neumann, S. Overall Survival Benefit with Tebentafusp in Metastatic Uveal Melanoma. *N. Engl. J. Med.* **2021**, *385* (13), 1196−1206.
(18) Woźniak, Ł.; Skąpska, S.; Marszałek, K. Ursolic Acid–A Pentacyclic Triterpenoid with a Wide Spectrum of Pharmacological Activities. *Molecules* **2015**, *20* (11), 20614.
(19) Zhang, Y.; Huang, L.; Shi, H.; Chen, H.; Tao, J.; Shen, R.; Wang, T. Ursolic acid enhances the therapeutic effects of oxaliplatin in colorectal cancer by inhibition of drug resistance. *Cancer Sci.* **2018**, *109* (1), 94−102.
(20) Park, J. H.; Kwon, H. Y.; Sohn, E. J.; Kim, K. A.; Kim, B.; Jeong, S. J.; Song, J. H.; Koo, J. S.; Kim, S. H. Inhibition of Wnt/β-catenin signaling mediates ursolic acid-induced apoptosis in PC-3 prostate cancer cells. *Pharmacol. Rep.* **2013**, *65* (5), 1366.
(21) Li, H.; Yu, Y.; Liu, Y.; Luo, Z.; Law, B. Y. K.; Zheng, Y.; Huang, X.; Li, W. Ursolic acid enhances the antitumor effects of sorafenib associated with Mcl-1-related apoptosis and SLC7A11-dependent ferroptosis in human cancer. *Pharmacol. Res.* **2022**, *182*, 106306.
(22) Maksimenko, O.; Malinovskaya, J.; Shipulo, E.; Osipova, N.; Razzhivina, V.; Arantseva, D.; Yarovaya, O.; Mostovaya, U.; Khalansky, A.; Fedoseeva, V.; Alekseeva, A.; Vanchugova, L.; Gorshkova, M.; Kovalenko, E.; Balabanyan, V.; Melnikov, P.; Baklaushev, V.; Chekhonin, V.; Kreuter, J.; Gelperina, S. Doxorubicin-loaded PLGA nanoparticles for the chemotherapy of glioblastoma: Towards the pharmaceutical development. *Int. J. Pharm.* **2019**, *572*, 118733.
(23) Gu, P.; Wusiman, A.; Wang, S.; Zhang, Y.; Liu, Z.; Hu, Y.; Liu, J.; Wang, D. Polyethylenimine-coated PLGA nanoparticles-encapsulated Angelica sinensis polysaccharide as an adjuvant to enhance immune responses. *Carbohydr. Polym.* **2019**, *223*, 115128.
(24) Courant, T.; Bayon, E.; Reynaud-Dougier, H. L.; Villiers, C.; Menneteau, M.; Marche, P. N.; Navarro, F. P. Tailoring nanostructured lipid carriers for the delivery of protein antigens: Physicochemical properties versus immunogenicity studies. *Biomaterials* **2017**, *136*, 29−42.
(25) Feltrin, F. D. S.; Agner, T.; Sayer, C.; Lona, L. M. F. Curcumin encapsulation in functional PLGA nanoparticles: A promising strategy for cancer therapies. *Adv. Colloid Interface Sci.* **2022**, *300*, 102582.
(26) Ryu, S.; Park, S.; Lee, H. Y.; Lee, H.; Cho, C. W.; Baek, J. S. Biodegradable Nanoparticles-Loaded PLGA Microcapsule for the Enhanced Encapsulation Efficiency and Controlled Release of Hydrophilic Drug. *Int. J. Mol. Sci.* **2021**, *22* (6), 2792.
(27) Park, K. Cover Story Enhanced intrapericardial drug delivery by PLGA nanoparticles. *J. Controlled Release* **2017**, *262*, 357.
(28) Chen, Q.; Chen, J.; Yang, Z.; Xu, J.; Xu, L.; Liang, C.; Han, X.; Liu, Z. Nanoparticle-Enhanced Radiotherapy to Trigger Robust Cancer Immunotherapy. *Adv. Mater.* **2019**, *31* (10), No. e1802228.
(29) Ji, T.; Li, Y.; Deng, X.; Rwei, A. Y.; Offen, A.; Hall, S.; Zhang, W.; Zhao, C.; Mehta, M.; Kohane, D. S. Delivery of local anaesthetics by a self-assembled supramolecular system mimicking their interactions with a sodium channel. *Nat. Biomed. Eng.* **2021**, *5* (9), 1099−1109.
(30) Yang, L.; Li, C. [Preparation and Evaluation of Hemoglobin-Bovine Serum Albumin Nanoparticles with Red Blood Cell Membrane Directional Coating]. *J. Sichuan Univ.* **2021**, *52* (4), 624−629.
(31) Song, M.; Dong, S.; An, X.; Zhang, W.; Shen, N.; Li, Y.; Guo, C.; Liu, C.; Li, X.; Chen, S. Erythrocyte-biomimetic nanosystems to improve antitumor effects of paclitaxel on epithelial cancers. *J. Controlled Release* **2022**, *345*, 744−754.
(32) Richter, L. R.; Wan, Q.; Wen, D.; Zhang, Y.; Yu, J.; Kang, J. K.; Zhu, C.; McKinnon, E. L.; Gu, Z.; Qiang, L.; Pajvani, U. B. Targeted

https://doi.org/10.1021/acsomega.4c05209
ACS Omega 2024, 9, 41532−41543

Delivery of Notch Inhibitor Attenuates Obesity-Induced Glucose Intolerance and Liver Fibrosis. *ACS Nano* **2020**, *14* (6), 6878−6886.
(33) Srivastava, I.; Xue, R.; Jones, J.; Rhee, H.; Flatt, K.; Gruev, V.; Nie, S. Biomimetic Surface-Enhanced Raman Scattering Nanoparticles with Improved Dispersibility, Signal Brightness, and Tumor Targeting Functions. *ACS Nano* **2022**, *16* (5), 8051−8063.
(34) Cao, J. Y.; Dixon, S. J. Mechanisms of ferroptosis. *Cell. Mol. Life Sci.* **2016**, *73* (11−12), 2195−2209.
(35) Wang, H.; Cheng, Y.; Mao, C.; Liu, S.; Xiao, D.; Huang, J.; Tao, Y. Emerging mechanisms and targeted therapy of ferroptosis in cancer. *Mol. Ther.* **2021**, *29* (7), 2185−2208.
(36) Chen, X.; Li, J.; Kang, R.; Klionsky, D. J.; Tang, D. Ferroptosis: machinery and regulation. *Autophagy* **2021**, *17* (9), 2054−2081.
(37) Hao, J.; Zhang, W.; Huang, Z. Bupivacaine modulates the apoptosis and ferroptosis in bladder cancer via phosphatidylinositol 3-kinase (PI3K)/AKT pathway. *Bioengineered* **2022**, *13* (3), 6794−6806.
(38) Long, G. V.; Swetter, S. M.; Menzies, A. M.; Gershenwald, J. E.; Scolyer, R. A. Cutaneous melanoma. *Lancet* **2023**, *402* (10400), 485−502.
(39) Carvajal, R. D.; Piperno-Neumann, S.; Kapiteijn, E.; Chapman, P. B.; Frank, S.; Joshua, A. M.; Piulats, J. M.; Wolter, P.; Cocquyt, V.; Chmielowski, B.; Evans, T. J.; Gastaud, L.; Linette, G.; Berking, C.; Schachter, J.; Rodrigues, M. J.; Shoushtari, A. N.; Clemett, D.; Ghiorghiu, D.; Mariani, G.; Spratt, S.; Lovick, S.; Barker, P.; Kilgour, E.; Lai, Z.; Schwartz, G. K.; Nathan, P. Selumetinib in Combination With Dacarbazine in Patients With Metastatic Uveal Melanoma: A Phase III, Multicenter, Randomized Trial (SUMIT). *J. Clin. Oncol.* **2018**, *36* (12), 1232−1239.
(40) Robert, C.; Thomas, L.; Bondarenko, I.; O'Day, S.; Weber, J.; Garbe, C.; Lebbe, C.; Baurain, J.-F.; Testori, A.; Grob, J.-J.; Davidson, N.; Richards, J.; Maio, M.; Hauschild, A.; Miller, W. H.; Gascon, P.; Lotem, M.; Harmankaya, K.; Ibrahim, R.; Francis, S.; Chen, T.-T.; Humphrey, R.; Hoos, A.; Wolchok, J. D. Ipilimumab plus dacarbazine for previously untreated metastatic melanoma. *N. Engl. J. Med.* **2011**, *364* (26), 2517−2526.
(41) Robert, C.; Long, G. V.; Brady, B.; Dutriaux, C.; Di Giacomo, A. M.; Mortier, L.; Rutkowski, P.; Hassel, J. C.; McNeil, C. M.; Kalinka, E. A.; Lebbé, C.; Charles, J.; Hernberg, M. M.; Savage, K. J.; Chiarion-Sileni, V.; Mihalcioiu, C.; Mauch, C.; Arance, A.; Cognetti, F.; Ny, L.; Schmidt, H.; Schadendorf, D.; Gogas, H.; Zoco, J.; Re, S.; Ascierto, P. A.; Atkinson, V. Five-Year Outcomes With Nivolumab in Patients With Wild-Type BRAF Advanced Melanoma. *J. Clin. Oncol.* **2020**, *38* (33), 3937−3946.
(42) Jiang, X.; Stockwell, B. R.; Conrad, M. Ferroptosis: mechanisms, biology and role in disease. *Nat. Rev. Mol. Cell Biol.* **2021**, *22* (4), 266−282.
(43) Lei, G.; Zhang, Y.; Hong, T.; Zhang, X.; Liu, X.; Mao, C.; Yan, Y.; Koppula, P.; Cheng, W.; Sood, A. K.; Liu, J.; Gan, B. Ferroptosis as a mechanism to mediate p53 function in tumor radiosensitivity. *Oncogene* **2021**, *40* (20), 3533−3547.
(44) Liu, Y.; Wang, Y.; Yang, Y.; Weng, L.; Wu, Q.; Zhang, J.; Zhao, P.; Fang, L.; Shi, Y.; Wang, P. Emerging phagocytosis checkpoints in cancer immunotherapy. *Signal Transduct. Targeted Ther.* **2023**, *8* (1), 104.
(45) Jin, M. Z.; Jin, W. L. The updated landscape of tumor microenvironment and drug repurposing. *Signal Transduct. Targeted Ther.* **2020**, *5* (1), 166.
(46) Quail, D. F.; Joyce, J. A. Microenvironmental regulation of tumor progression and metastasis. *Nat. Med.* **2013**, *19* (11), 1423.
(47) Ma, X.; Xiao, L.; Liu, L.; Ye, L.; Su, P.; Bi, E.; Wang, Q.; Yang, M.; Qian, J.; Yi, Q. CD36-mediated ferroptosis dampens intratumoral CD8(+) T cell effector function and impairs their antitumor ability. *Cell Metabol.* **2021**, *33* (5), 1001.e5−1012.e5.
(48) van Vlerken-Ysla, L.; Tyurina, Y. Y.; Kagan, V. E.; Gabrilovich, D. I. Functional states of myeloid cells in cancer. *Cancer cell* **2023**, *41* (3), 490−504.
(49) Tang, C.; Wang, C.; Zhang, Y.; Xue, L.; Li, Y.; Ju, C.; Zhang, C. Recognition, Intervention, and Monitoring of Neutrophils in Acute Ischemic Stroke. *Nano Lett.* **2019**, *19* (7), 4470−4477.

https://doi.org/10.1021/acsomega.4c05209
ACS Omega 2024, 9, 41532−41543